Frontiers in Computing and Intelligent Systems
ISSN: 2832-6024 | Vol. 11, No. 1, 2025

Research on Sensorless FOC Method of PMSM based on ADRC

Xin Zhang [1, 2], Miao Huang [1, *], Lili Tao [1], Shuping Zhang [1], Zhihua Hu [1]

[1] School of Intelligent Manufacturing and Control Engineering, Shanghai Polytechnic University, Shanghai, 201209, China
[2] Vocational & Technical Teacher Education School, Shanghai Polytechnic University, Shanghai, 201209, China

[*] **Corresponding author**: Miao Huang (Email: huangmiao@sspu.edu.cn)

Abstract: This paper addresses the issues of low observer estimation accuracy, high speed overshoot, narrow speed range, and poor anti-disturbance performance in traditional sensorless Permanent Magnetic Synchronous Motor (PMSM) Field Oriented Control (FOC) systems. It proposes two control methods combining the Extended Kalman Filter (EKF) observer with Linear Active Disturbance Rejection Control (LADRC) and Nonlinear Active Disturbance Rejection Control (NLADRC). The EKF is used to estimate rotor position and speed, while LADRC and NLADRC controllers compensate for load disturbances in the speed loop. EKF outputs are used for feedforward compensation in the current loop, eliminating the coupling between d-axis and q-axis voltages. Simulation results show that both methods offer strong anti-disturbance performance, a wide speed range, strong speed overshoot suppression, and accurate estimation of motor speed and rotor position, thereby enhancing the operational stability of the PMSM system.

Keywords: PMSM; EKF; ADRC; FOC; Voltage Feed-forward Control; Sensorless Control.

1. Introduction

PMSM (Permanent Magnet Synchronous Motors) are widely used in industrial control, medical machinery, automotive manufacturing, and other fields due to their advantages such as simple structure, high power density, and low manufacturing cost. Traditional PMSM control strategies include sine pulse width modulation (SPWM), Field-Oriented Control (FOC), Direct Torque Control (DTC), etc. Among these, FOC technology offers advantages like fast response, high voltage utilization, a wide speed range, and high control accuracy. However, traditional FOC relies on position sensors to obtain rotor angle, which increases motor cost and size, and significantly reduces motor adaptability. To solve these issues, sensorless FOC has emerged. Sensorless FOC utilizes state observation algorithms to establish rotor speed and position observers to replace position sensors.

Common state observation algorithms used in sensorless FOC include the Extended Kalman Filter (EKF) observer, Luenberger observer, and others. The EKF observer is based on the minimum variance estimation theory and achieves accurate estimation of state variables through data fusion. It can operate over a wide speed range, has filtering capabilities, and is adaptive with low requirements for initial state estimation. For instance, Changchang Jiang et al. proposed a sensorless vector control strategy based on the EKF observer and used a Luenberger observer to track load changes, providing feedforward compensation for the current loop PI controller, thereby enhancing the tracking and disturbance rejection capabilities of the EKF observer [1]. Shijiao Wang et al. proposed a particle swarm optimization-based fuzzy PI control method, which improves the dynamic and disturbance rejection performance of the system[2]. Weilin Yang et al. proposed a control strategy for PMSM based on an improved neural network[3]. Lin Liu et al. proposed a PI control parameter self-tuning and optimization method combining model and rule-based approaches[4]. Jiaxuan Li et al. designed an adaptive PI controller based on BP neural networks and improved the traditional FOC model to enhance system response speed and robustness[5]. These scholars have used modern control theory and intelligent algorithms to improve traditional PI controllers. Although the improvements are significant, the contradiction between overshoot and speed remains unresolved.

Furthermore, the rapid development of modern control theory has led to the design of various motor control algorithms, such as sliding mode control, model reference adaptive control, robust control, internal model control, and disturbance-free control, to replace traditional PI control [6,7,8]. In the 1980s, Professor Jingqing Han analyzed the drawbacks of modern control theory's over-reliance on mathematical models and studied traditional control methods for error suppression through system feedback[9]. In 1998, he proposed the Active Disturbance Rejection Control (ADRC) theory and published a monograph[10]. This control method not only has a simple algorithm but also detects and compensates for internal and external disturbances, enabling the system to promptly respond to disturbances and parameter changes. ADRC is characterized by strong disturbance suppression, high robustness, and good operability[11,12]. For example, Shiwei Chi et al. proposed a feedforward compensation-based ADRC strategy for PMSMs to suppress speed fluctuations caused by sudden load torque changes, optimizing the control performance[13]. Zixin Li et al. proposed a parameter self-tuning strategy based on BP neural networks to address the difficulty of tuning ADRC parameters, effectively reducing the complexity of parameter tuning while improving system performance and lowering the difficulty of applying ADRC in engineering[14]. Yicheng Wang et al. proposed an improved PMSM weak magnetic ADRC method to meet the high-speed, high-stability, and fast-response requirements of multi-electric aircraft, and demonstrated its superior performance through comparisons with traditional weak magnetic control and ADRC weak magnetic control [15].

This paper proposes a sensorless ADRC strategy for

PMSMs based on the EKF observer to address issues such as load disturbance impact on PMSM system stability, the trade-off between response speed and overshoot in PMSM systems, and the high cost and poor adaptability caused by position sensors. The speed loop replaces the PI controller with an ADRC controller, and the EKF observer estimates speed and angle. The current loop implements decoupling of the d-axis and q-axis voltages through feedforward compensation. Finally, comparative experiments are conducted on three control strategies: PI + FOC + EKF, LADRC + FOC + EKF, and NLADRC + FOC + EKF, to verify the control effect of the proposed method.

2. Mathematical Model of PMSM

The following assumptions are made for the PMSM model:

(1) The rotor permanent magnet's magnetic field distribution is sinusoidal.
(2) The back electromotive force (EMF) in the stator windings is sinusoidal.
(3) The stator core saturation, as well as eddy current and hysteresis losses in the core, are neglected.
(4) There are no damper windings on the rotor.

The stator voltage equation of the PMSM in a synchronous rotating coordinate system is:

$$\begin{cases} u_d = Ri_d + \dfrac{d\varphi_d}{dt} - \omega_e\varphi_q \\ u_q = Ri_q + \dfrac{d\varphi_q}{dt} + \omega_e\varphi_d \end{cases} \tag{1}$$

The flux linkage equations are as follows:

$$\begin{cases} \varphi_d = L_d i_d + \varphi_f \\ \varphi_q = L_q i_q \end{cases} \tag{2}$$

u_d and $u_q$are the voltage components of the stator in the $d-$axis and $q-$axis, respectively; i_d and i_q are the current components of the stator in the $d-$axis and $q-$axis, respectively; φ_d and φ_q are the flux linkage components of the stator in the $d-$axis and $q-$axis, respectively; L_d and L_q are the inductance components of the stator in the $d-$axis and $q-$axis, respectively; R, ω_e and φ_f are the stator resistance, electrical angular velocity, and permanent magnet flux linkage, respectively.

The electromagnetic torque equation of the motor is:

$$T_e = P_n(\varphi_d i_q - \varphi_q i_d) = P_n[\varphi_f i_q + (L_d - L_q) i_d i_q] \tag{3}$$

P_n is the pole number, and T_e is the electromagnetic torque.

The conversion relationships between the mechanical angular velocity (rad·s^{-1}), mechanical speed (r·min^{-1}), electrical angular velocity (rad·s^{-1}), and electrical angle (rad) are as follows:

$$\begin{cases} \omega_e = P_n\omega_m \\ N_r = \dfrac{30}{\pi}\omega_m \\ \theta_e = \int \omega_e dt \end{cases} \tag{4}$$

ω_m is the mechanical angular velocity of the motor, N_r is the mechanical speed of the motor, and θ_e is the electrical angle of the motor.

The mechanical motion equation of the motor is:

$$J\frac{d\omega_m}{dt} = T_e - T_L - B\omega_m \tag{5}$$

J is the moment of inertia; B is the damping coefficient; T_L is the load torque.

This paper combines the EKF algorithm and ADRC theory to propose a sensorless control method for PMSM. The rotor position and speed are estimated through EMF, enhancing the system's stability and accuracy, while addressing the trade-off between response speed and overshoot.

3. The Design of the Improved FOC Control Scheme

The core of FOC is to use coordinate transformation to degrade and decouple the complex and strongly coupled PMSM model in the natural coordinate system. Ultimately, the motor model is transformed into the PMSM model shown in equations (1) to (5), achieving decoupled control of the excitation current and torque current.

The main steps are as follows:

(1) The equal-magnitude Clarke transform converts the sampled three-phase current into a two-phase stationary coordinate system, represented as i_α, i_β. The formula for the equal-magnitude Clarke transform is as follows:

$$\begin{cases} i_\alpha = \dfrac{2}{3}(i_a \times \cos 0^\circ + i_b \times \cos 120^\circ + i_c \times \cos 240^\circ) \\ i_\beta = \dfrac{2}{3}(i_a \times \sin 0^\circ + i_b \times \sin 120^\circ + i_c \times \sin 240^\circ) \end{cases} \tag{6}$$

After simplification, the Clarke transform formula becomes:

$$\begin{cases} i_\alpha = \dfrac{2}{3}(i_a - \dfrac{1}{2}i_b - \dfrac{1}{2}i_c) \\ i_\beta = \dfrac{2}{3}(\dfrac{\sqrt{3}}{2}i_b - \dfrac{\sqrt{3}}{2}i_c) \end{cases} \tag{7}$$

(2) Through the Park transform, using the rotor angle information θ, obtained by the observer or sensor, the current components i_α, i_β in the $\alpha-\beta$ coordinate system are transformed into the $d-q$ coordinate system, which is aligned with the rotor flux position, resulting in i_d and i_q. The Park transform formula is as follows:

$$\begin{cases} i_d = i_\alpha \times \cos\theta + i_\beta \times \sin\theta \\ i_q = -i_\alpha \times \sin\theta + i_\beta \times \cos\theta \end{cases} \tag{8}$$

(3) The differences between i_d, i_q and the current reference values i_{dref}, i_{qref} from the speed loop output are sent into the current loop controller to calculate the next voltage vectors V_d and V_q. i_{dref} aligns with the rotor flux to control the flux, and is generally set to 0. i_{qref} is perpendicular to the rotor flux to control the output torque.

(4) Using the inverse Park transformation, the newly estimated electrical angle θ is used to transform V_d and V_q into the two-phase stationary reference frame, resulting in V_α and V_β. The formula for the inverse Park transformation is as follows:

$$\begin{cases} V_\alpha = V_d \times \cos\theta - V_q \times \sin\theta \\ V_\beta = V_d \times \sin\theta + V_q \times \cos\theta \end{cases} \tag{9}$$

(5) Through the Clarke inverse transformation, V_α and V_β are converted into V_a, V_b and V_c in the natural coordinate system, and then sent to the SVPWM module to generate the SVPWM wave, which is output to the three-phase inverter bridge. The formula for the Clarke inverse transformation is as follows:

$$\begin{cases} V_a = V_\alpha \\ V_b = -V_\alpha \times \sin 30^\circ + V_\beta \times \cos 30^\circ \\ V_c = -V_\alpha \times \sin 30^\circ - V_\beta \times \cos 30^\circ \end{cases} \quad (10)$$

After simplification, it becomes:

$$\begin{cases} V_a = V_\alpha \\ V_b = -\frac{1}{2}V_\alpha + \frac{\sqrt{3}}{2}V_\beta \\ V_c = -\frac{1}{2}V_\alpha - \frac{\sqrt{3}}{2}V_\beta \end{cases} \quad (11)$$

(6) In the speed loop, the speed information ω obtained by the observer and the error between the given speed reference ω_{ref} are fed into the speed loop controller to obtain i_{qref}.

From Equation (3), it can be seen that the motor model after the FOC transformation is not completely decoupled, as V_d and V_q contain components of each other. This results in the inability to achieve independent control and causes high-frequency oscillations. Therefore, by introducing feedforward compensation signals equal to the coupling terms into the outputs of the $d-$axis and $q-$axis controllers, decoupled control of torque and magnetizing current is achieved. The control system block diagram is shown in Figure 1:

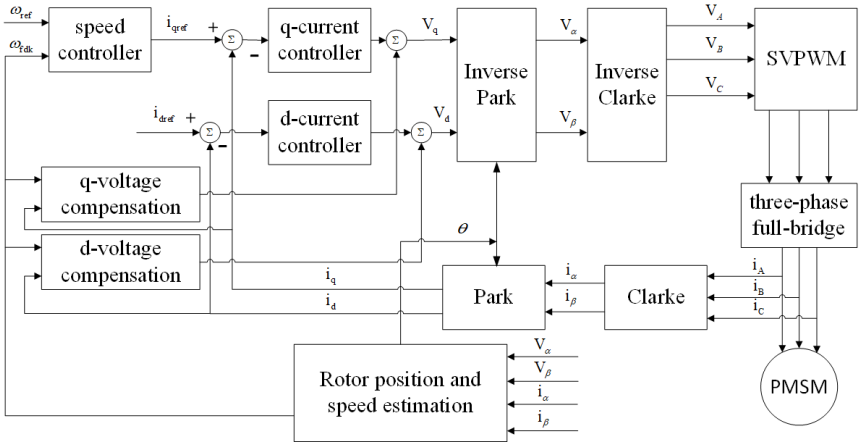

Figure 1. Block diagram of the improved FOC control system

4. Design of Speed and Position Observer Based on EKF Algorithm

The PMSM system is a typical nonlinear system, and its state-space expression is:

$$x_{[k]} = f(x_{[k-1]}, u_{[k-1]}, w_{[k-1]}) \quad (12)$$

$$z_{[k]} = h(x_{[k]}, v_{[k]}) \quad (13)$$

In this expression, $f(\cdot)$ and $h(\cdot)$ are nonlinear equations, $w \sim N(0, Q)$ and $v \sim N(0, R)$ represent the system noise and measurement noise, respectively, which follow a normal distribution.

4.1. The Core Algorithm of the EKF Observer

The EKF observation algorithm is divided into two main steps: prediction and correction:

Prediction stage (time update stage):

(1) Calculate the prior state estimate.

$$\hat{x}_{[k]}^{-} = f(\hat{x}_{[k-1]}, u_{[k-1]}, 0) \quad (14)$$

$\hat{x}_{[k]}^{-}$ is the prior state estimate at time k, $\hat{x}_{[k-1]}$ is the posterior state estimate at time k-1, and $u_{[k-1]}$ is the system input at time k-1. In the prior state estimation, the system error is assumed to be zero. The initial state estimate is denoted as $\hat{x}_{[0]}$.

(2) Calculate the Jacobian matrix (linearization of the nonlinear system).

The EKF algorithm uses the Taylor series expansion method to linearize the nonlinear system. The equation (12) is expanded in a Taylor series around the posterior state estimate $\hat{\boldsymbol{x}}_{[k-1]}$, ignoring the higher-order terms in the Taylor expansion and assuming that the system error around $\hat{\boldsymbol{x}}_{[k-1]}$ is zero.

$$\begin{aligned} x_{[k]} &= f(x_{[k-1]}, u_{[k-1]}, w_{[k-1]}) \\ &\approx f(\hat{x}_{[k-1]}, u_{[k-1]}, 0) + A_{[k]}(x_{[k-1]} - \hat{x}_{[k-1]}) + W_{[k]}(w_{[k-1]} - 0) \end{aligned} \quad (15)$$

$$A_{[k]} = \frac{\partial f}{\partial x}(\hat{x}_{[k-1]}, u_{[k-1]}, 0) \quad (16)$$

$$W_{[k]} = \frac{\partial f}{\partial w}(\hat{x}_{[k-1]}, u_{[k-1]}, 0) \quad (17)$$

Equations (16) and (17) represent the Jacobian matrices of the first-order partial derivatives of $f()$ with respect to the system state x and the system error w, respectively.

(3) Calculate the covariance matrix of the prior state estimate error.

$$P_{[k]}^{-} = A_{[k]}P_{[k]}A_{[k-1]}^{T} + W_{[k]}QW_{[k]}^{T} \quad (18)$$

The covariance matrix of the system noise and the covariance matrix of the initial state estimation error are denoted as Q and $P_{[0]}$.

Correction stage (measurement update):

(1) Calculate the Jacobian matrix.

Expand equation (13) around $\hat{x}_{[k]}^{-}$, that is,

$$z_{[k]} = h(x_{[k]}, v_{[k]}) \approx h(\hat{x}_{[k]}^{-}, 0) + H_{m[k]}(x_{[k]} - \hat{x}_{[k]}^{-}) + V_{[k]}(v_{[k]} - 0) \quad (19)$$

$$H_{m_{[k]}} = \frac{\partial h}{\partial x}(\hat{x}_{[k]}^{-}, 0) \quad (20)$$

$$V_{[k]} = \frac{\partial h}{\partial v}(\hat{x}_{[k]}^{-}, 0) \quad (21)$$

$\boldsymbol{H}_{m_{[k]}}$ and $\boldsymbol{V}_{[k]}$ are the Jacobian matrices of $\boldsymbol{h}$ with respect to $\boldsymbol{x}$ and $\boldsymbol{v}$, respectively.

Equations (15) and (19) form the system state-space equations after linearization, which can be simplified as:

$$x_{[k]} = A_{[k]}x_{[k-1]} + W_{[k]}w_{[k-1]} + (\hat{x}_{[k]}^{-} - A_{[k]}\hat{x}_{[k-1]}) \quad (22)$$

$$z_{[k]} = H_{m_{[k]}}x_{[k]} + V_{[k]}v_{[k]} + (h(\hat{x}_{[k]}^{-}, 0) - H_{m_{[k]}}\hat{x}_{[k]}^{-}) \quad (23)$$

This is a linear equation, so the noise

$W_{[k]}w_{[k-1]} \sim N(0, W_{[k]}QW_{[k]}^T)$, $V_{[k]}v_{[k]} \sim N(0, V_{[k]}RV_{[k]}^T)$ are assumed to follow a normal distribution.

(2) Calculate the Kalman gain.

$$K_{[k]} = \frac{P_{[k]}^- H_{m_{[k]}}^T}{H_{m_{[k]}} P_{[k]}^- H_{m_{[k]}}^T + V_{[k]} R V_{[k]}^T} \tag{24}$$

(3) Calculate the posterior state estimate.

$$\hat{x}_{[k]} = \hat{x}_{[k]}^- + K_{[k]}[z_{[k]} - h(\hat{x}_{[k]}^-, 0)] \tag{25}$$

(4) Update the posterior state estimate error covariance matrix.

$$P_{[k]} = (I - K_{[k]} H_{m_{[k]}}) P_{[k]}^- \tag{26}$$

Equations (14) and (25) use the noiseless nonlinear system model to obtain the prior and posterior estimates. Equations (18), (24), and (25) all use the linearized model for calculations.

4.2. Design of the Speed and Position Observer

The EKF is a state observer that relies on the motor model and can perform estimations in both synchronous rotating and stationary reference frames. The synchronous reference frame requires multiple coordinate transformations and involves trigonometric functions (sine and cosine), which increase nonlinearity and computational complexity, thereby extending the recursion time. In contrast, the stationary reference frame only requires a Clarke transformation, which reduces the model's nonlinearity and improves estimation accuracy. The structure diagram of the EKF observer is shown in Figure 2.

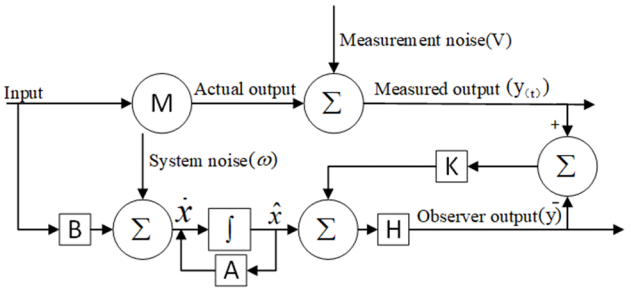

Figure 2. Block Diagram of Extended Kalman Filter Observer Structure

The voltage equations of the PMSM in the $\alpha - \beta$ stationary reference frame is:

$$u_\alpha = Ri_\alpha + L_s \frac{di_\alpha}{dt} - \omega_e \varphi_f \sin\theta_e \tag{27}$$

$$u_\beta = Ri_\beta + L_s \frac{di_\beta}{dt} + \omega_e \varphi_f \cos\theta_e \tag{28}$$

The relationship between the electrical angle and the electrical angular velocity is as follows:

$$\begin{cases} \frac{d\omega_e}{dt} = 0 \\ \frac{d\theta_e}{dt} = \omega_e \end{cases} \tag{29}$$

Equations (27), (28), and (29) represent the state equations of the PMSM system in the $\alpha - \beta$ stationary reference frame.

Let $\boldsymbol{x} = [i_\alpha, i_\beta, \omega_e, \theta_e]^T$ represent the state variables of the observation system, $\boldsymbol{u} = [u_\alpha, u_\beta]^T$ the input of the observation system, and $\boldsymbol{y} = [i_\alpha, i_\beta]^T$ the output of the observation system. The state equations of the PMSM can then be written as:

$$\dot{x} = f(x) + Bu + \omega \tag{30}$$

In the equation: ω represents the system noise. $\boldsymbol{B} = \begin{bmatrix} \frac{1}{L_s} & 0 \\ 0 & \frac{1}{L_s} \\ 0 & 0 \\ 0 & 0 \end{bmatrix}$ represents the input matrix, $f(x) = \begin{bmatrix} -\frac{R}{L_s} i_\alpha + \omega_e \frac{\varphi_f}{L_s} \sin\theta_e \\ -\frac{R}{L_s} i_\beta - \omega_e \frac{\varphi_f}{L_s} \cos\theta_e \\ 0 \\ \theta_e \end{bmatrix}$.

Since i_α and i_β can be directly measured, the measurement equation is defined as:

$$y = Cx + v \tag{31}$$

In the equation: $\boldsymbol{C} = \begin{bmatrix} 1 & 0 & 0 & 0 \\ 0 & 1 & 0 & 0 \end{bmatrix}$ represents the output matrix.

The Jacobian matrix of the system's state equations is:

$$F(k) = \frac{\partial f(x)}{\partial x}|_{x=\hat{x}_{(k)}} = \begin{pmatrix} -\frac{R}{L_s} & 0 & \frac{\varphi_f}{L_s}\sin\hat{\theta}_{e(k)} & \hat{\omega}_e \frac{\varphi_f}{L_s}\cos\hat{\theta}_{e(k)} \\ 0 & -\frac{R}{L_s} & -\frac{\varphi_f}{L_s}\cos\hat{\theta}_{e(k)} & \hat{\omega}_e \frac{\varphi_f}{L_s}\sin\hat{\theta}_{e(k)} \\ 0 & 0 & 0 & 0 \\ 0 & 0 & 1 & 0 \end{pmatrix}$$

4.3. The Selection of the Noise Covariance Matrix

In the EKF algorithm's estimation process, the covariance matrices of the noise ω and v are required. The definitions of the covariance matrices Q and R are as follows:

$$\begin{cases} Q = E\{WW^T\} \\ R = E\{VV^T\} \end{cases} \tag{32}$$

The initial state random vector $\boldsymbol{x}_{(0)}$ and the noise vectors V and W are mutually independent.

Since the off-diagonal elements have a negligible impact on the system, Q, R and P_0 are generally taken as diagonal matrices.

From equations (18) and (24), it is known that the Q matrix and the R matrix adjust the Kalman gain, affecting the weight of the estimated values and the measurement values. Increasing Q leads to a higher Kalman gain, increasing the weight of the measurement values; increasing R leads to a lower Kalman gain, increasing the weight of the estimated values. A larger Q allows the system to converge faster but becomes less reliable; a larger R causes the observer's output to lag, deteriorating dynamic performance. The PMSM model is complex, and selecting the appropriate Q and R matrices is difficult. Particle swarm optimization (PSO), grey wolf optimization (GWO), and other algorithms can be used to optimize the elements of the Q and R matrices.

In simulations, the EKF outputs the optimal estimated values of the motor model, not the actual optimal estimates of the real motor system, so there may be some deviation between the estimated values and the actual feedback values.

5. Design of the Speed Loop Controller Based on ADRC

The tracking differentiator (TD), extended state observer

(ESO), and nonlinear state error feedback control law (NLSEF) form the active disturbance rejection controller (ADRC) [16]. Its structure is shown in Figure 3.

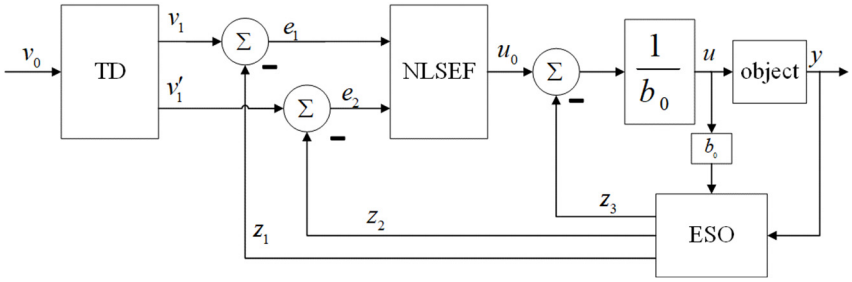

Figure 3. NLADRC controller structure diagram

The TD quickly tracks the desired signal using the fastest synthesis function and synchronizes the output differential signal, reducing noise amplification and steady-state errors. By performing multi-order planning on the desired signal, it reduces the impact of the input signal on the system, achieving smooth input and thereby reducing overshoot.

The discrete mathematical model of the TD is:

$$\begin{cases} fh = fhan(x_1(k) - v(k), x_2(k), r_0, h_0) \\ x_1(k+1) = x_1(k) + hx_2(k) \\ x_2(k+1) = x_2(k) + hfh \end{cases} \tag{33}$$

Where:

$$fhan(x_1, x_2, r_0, h_0) = \begin{cases} d = r_0 h_0^2 \\ a_0 = h_0 x_2 \\ y = x_1 + a_0 \\ a_1 = \sqrt{d(d + 8|y|)} \\ a_2 = a_0 + \dfrac{sign(y)(a_1 - d)}{2} \\ S_y = \dfrac{sign(y + d) - sign(y - d)}{2} \\ a = (a_0 + y - a_2)S_y + a_2 \\ S_a = \dfrac{sign(a + d) - sign(a - d)}{2} \\ fhan = -r\left[\dfrac{a}{d} - sign(a)\right]S_a - r_0 sign(a) \end{cases} \tag{34}$$

x_1, x_2 are the target control variables and their derivatives, r_0, h_0 are the control parameters of the function. r_0 controls the tracking speed: the larger r_0 is, the faster the tracking, but the noise amplification effect and overshoot will also increase. If r_0 is too large, it may cause system oscillation. Typically, in the PMSM system, $r_0 \in (0,1000]$ is acceptable. h_0 controls the internal iteration step size of $fhan$, which is similar to the system sampling period. To avoid noise amplification, h_0 is usually selected as an integer multiple of the sampling period.

The discrete mathematical model of the nonlinear Extended State Observer (ESO) is:

$$\begin{cases} e(k) = z_1(k) - y(k) \\ z_1(k+1) = z_1(k) + h[z_2(k) - \beta_{01}e(k)] \\ z_2(k+1) = z_2(k) + h[z_3(k) - \beta_{02}fal(e, a_1, \delta) + bu] \\ z_3(k+1) = z_3(k) - h\beta_{03}fal(e, a_2, \delta) \end{cases} \tag{35}$$

Where, fal is the nonlinear function:

$$fal(x, a, \delta) = \begin{cases} \dfrac{x}{\delta^{(1-a)}}, |x| \le \delta \\ sign(x)|x|^a, |x| > \delta \end{cases} \tag{36}$$

The function $fal(x, a, \delta)$ ensures that the ESO state variables z_i can closely approximate the system state variables x_i, and have a larger adaptation range. The parameters that need to be tuned in equation (35) include: a_1, a_2, δ, β_{01}, β_{02}, β_{03}, b. a_1 and a_2 are nonlinear factors, with values in the range $a_i \in (0,1]$, and $a_2 = \frac{1}{2}a_1$. δ is the filtering factor, with values in the range $\delta \in (0,0.1]$. The error gain parameters β_{01}, β_{02}, β_{03} need to be analyzed based on the specific system characteristics. Generally, the relationship among their values is:

$$\begin{cases} \beta_{02} = 10\beta_{01} \\ \beta_{03} = {\beta_{01}}^2 \end{cases} \tag{37}$$

The compensation factor b needs to be analyzed based on the output waveform of the controller. Increasing b can reduce chattering caused by an increased controller bandwidth, but an excessively large b will decrease the disturbance compensation amount, reducing the effectiveness of disturbance suppression.

The combination relationship of the NLSEF is:

$$u_0 = \beta_1 fal(e_1, a_1, \delta) + \beta_2 fal(e_2, a_2, \delta) \tag{38}$$

The tunable parameters in NLSEF include the error gains β_1 and β_2. Increasing β_1 and β_2 accelerates the speed response, but excessive values can lead to overshoot, while smaller values may result in steady-state errors in speed. During parameter tuning, increments are usually made in orders of magnitude until overshoot appears, and then the values are gradually reduced to the optimal level.

The tuning methods for a_1, a_2 and δ are similar to those used in ESO, but in NLSEF, the value range of a_1 is $a_1 \in (0,1]$, and for a_2, $a_2 \in [1, +\infty]$.

Linear Active Disturbance Rejection Control (LADRC) simplifies the NLADRC by replacing the TD and NLSEF with PD control. This approach associates the tunable parameters with the frequency-domain bandwidth of the controller, simplifying the controller design process. The basic structure of LADRC is shown in Figure 4.

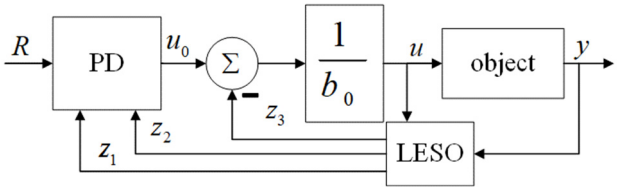

Figure 4. LADRC controller structure diagram

The parameter tuning of NLADRC and LADRC controllers is relatively challenging. Optimization algorithms such as Whale Optimization Algorithm (WOA), Grey Wolf Optimization (GWO), and Reinforcement Learning (RL) can be used for automatic parameter tuning, significantly reducing the workload involved in the tuning process.

6. Simulation Testing and Results Analysis

6.1. Construction of the Simulink Simulation Model

Based on the above content, construct a graphical simulation control model for PMSM in the MATLAB/Simulink environment. Perform comparative simulation experiments for three control systems: PI+EKF, LADRC+EKF, and NLADRC+EKF. The model uses a fixed step size of 2e-6s, the ode23tb solver, and a simulation duration of 0.6s. Tables 1~4 detail the parameters of each part of the model, and the model structure is illustrated in Figures 5~7.

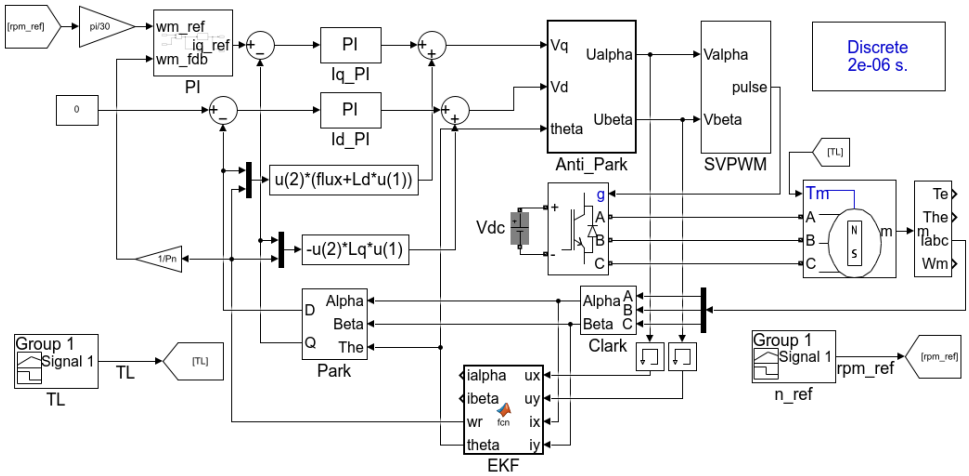

Figure 5. Simulation model diagram of PI+EKF control system

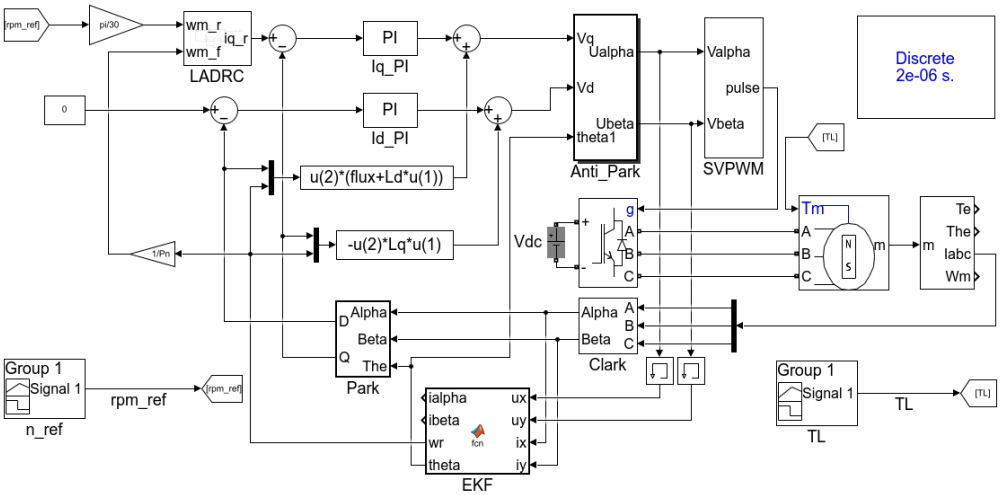

Figure 6. Simulation model diagram of LADRC+EKF control system

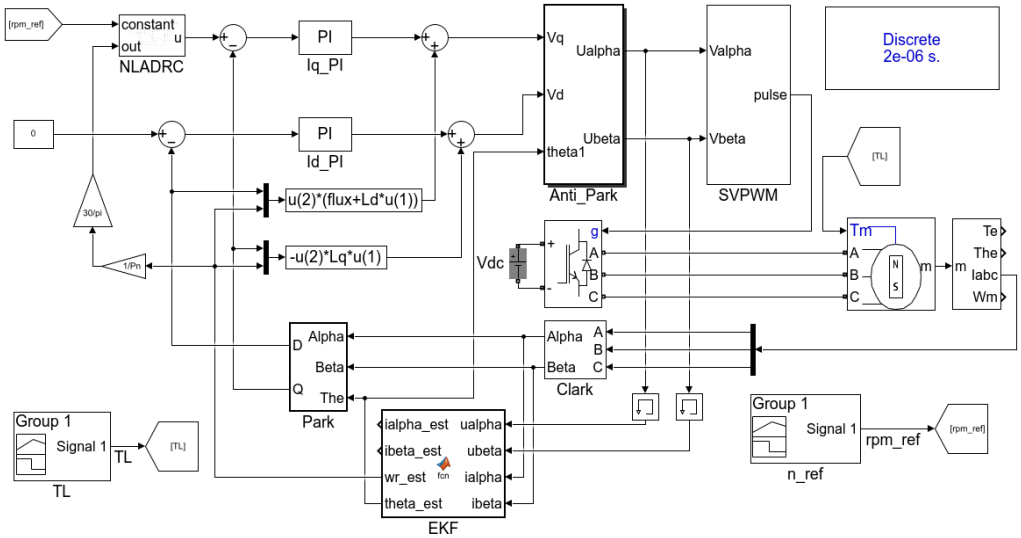

Figure 7. Simulation model diagram of NLADRC+EKF control system

Table 1. Motor Simulation Model Parameter Table

Name	Value
DC-side supply voltage (V_{dc}/V)	311
Number of motor pole pairs (P_n)	4
Per-phase stator resistance (R/Ω)	2.8750
Moment of inertia J/(kg·m^{-2})	0.001
Stator inductance L/mH	0.0085
Rotor flux linkage ψ/Wb	0.175

Table 2. ESO parameter table

Name	Value
Q_{11}	1.5
Q_{22}	1.5
Q_{33}	26
Q_{44}	0.2
P_{11}	0.1
P_{22}	0.1
R_{11}	20.9
R_{22}	20.9

Table 3. LADRC parameter table

Name	Value
b_0	1096
K_p	0.17
$\boldsymbol{\beta_1}$	3600
$\boldsymbol{\beta_2}$	3239049

Table 4. NLADRC parameter table

Name	Value
R_0	600
h_0	0.01
a_1	0.5
a_2	0.25
$\boldsymbol{\delta}$	0.015
$\boldsymbol{\beta_{01}}$	300
$\boldsymbol{\beta_{02}}$	3520
$\boldsymbol{\beta_{03}}$	115300
$\boldsymbol{b}$	300
$\boldsymbol{\beta_1}$	11000
$\boldsymbol{\beta_2}$	60

6.2. Simulation Results

The initial speed for all three models is set to 1500 RPM. At 0.2s, the load increases by 2 N·m, and at 0.4s, the speed is reduced to 1000 RPM. The speed waveform comparison is shown in Figure 8.

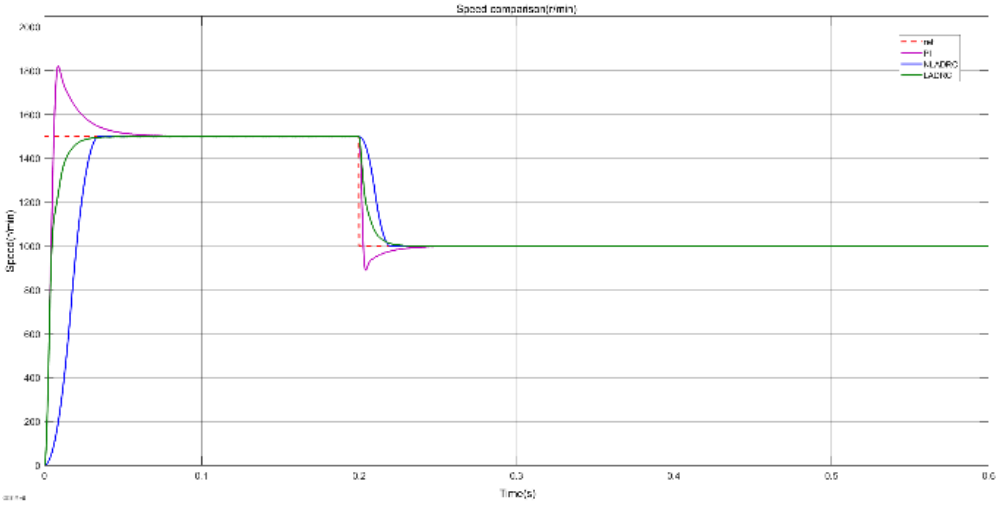

Figure 8. Comparison of motor speed waveforms for the three control strategies

As shown in the figure, when the reference speed is set to 1500 RPM within the first 0.4 seconds: PI+EKF system overshoots to 1821 RPM at 0.0089 seconds and stabilizes at 1500 RPM in 0.1 seconds; LADRC+EKF system exhibits no overshoot and stabilizes at 0.047 seconds; NLADRC+EKF system also shows no overshoot and stabilizes at 0.035 seconds.

At 0.2 seconds, when a 2 N·m load is applied: PI+EKF system takes 0.07 seconds to return to 1500 RPM; LADRC+EKF system takes 0.016 seconds; NLADRC+EKF system takes only 0.002 seconds.

At 0.4 seconds, when the reference speed drops to 1000 RPM: PI+EKF system responds the fastest but overshoots to 906 RPM and stabilizes in 0.053 seconds; LADRC+EKF and NLADRC+EKF systems show no overshoot and stabilize in 0.039 seconds and 0.02 seconds, respectively.

Figures 9 to 11 illustrate the current waveforms of the PI+EKF, LADRC+EKF, and NLADRC+EKF systems, respectively.

From Figures 9 to 11, under a load of 3 N·m during motor start-up: PI+EKF system's current stabilizes after 0.052 seconds, with significant overshoot; LADRC+EKF system exhibits reduced current overshoot and stabilizes after 0.035 seconds; NLADRC+EKF system shows the smallest current overshoot and stabilizes after 0.033 seconds.

When the reference speed drops to 1000 RPM at 0.4 seconds: PI+EKF system's current stabilizes in 0.024 seconds; LADRC+EKF system stabilizes in 0.02 seconds; NLADRC+EKF system stabilizes in 0.022 seconds.

In summary, the NLADRC+EKF system demonstrates superior performance but poses greater challenges in parameter tuning. The LADRC+EKF system performs

slightly less effectively but is easier to tune, making it more convenient for engineering applications.

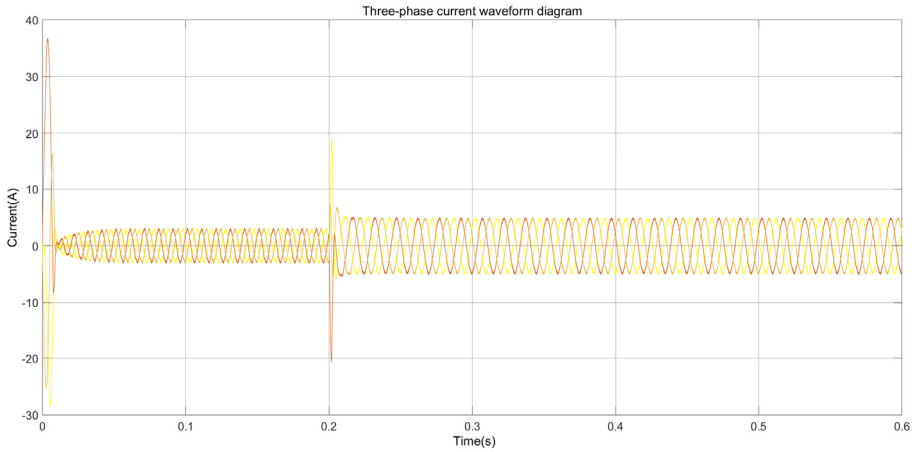

Figure 9. current waveform based on PI+EKF system

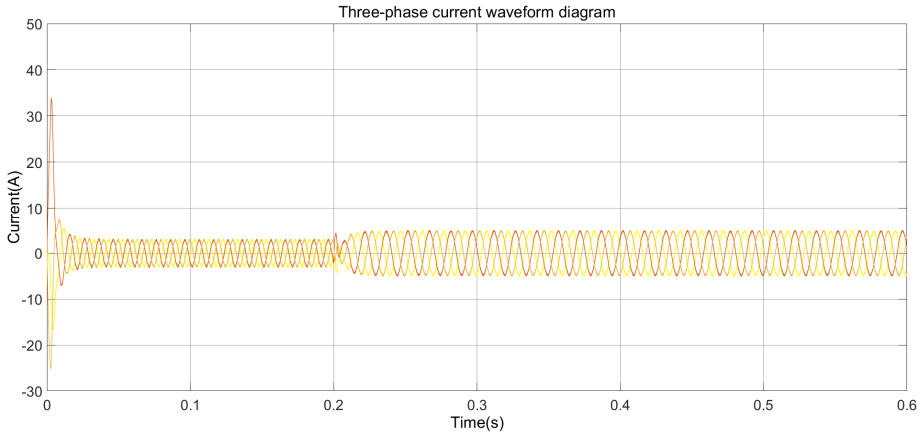

Figure 10. current waveform based on LADRC+EKF system

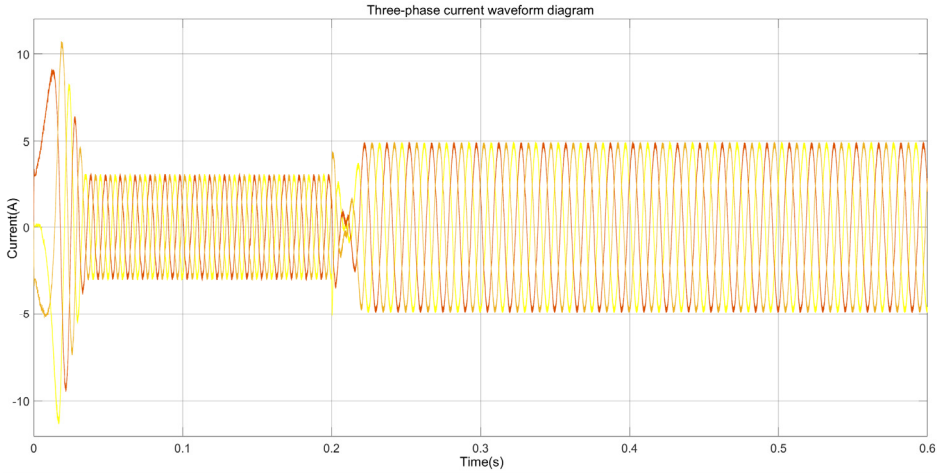

Figure 11. current waveform based on NLADRC+EKF system

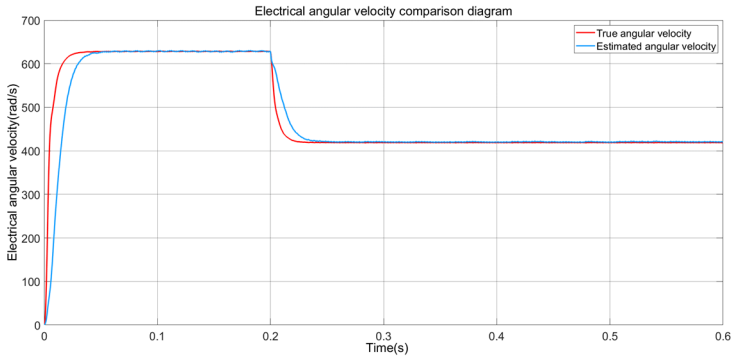

Figure 12. Comparison of EKF estimated angular velocity and the real angular velocity

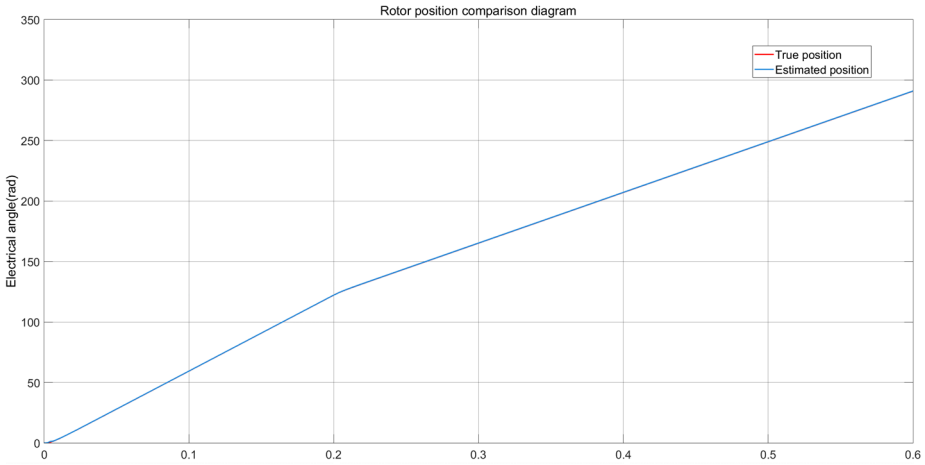

Figure 13. Comparison of the EKF estimated rotor electrical angle with the true electrical angle

Figures 12 and 13 respectively show the comparison between the EKF-estimated and actual angular velocity, as well as the comparison between the actual and estimated electrical angles.

Figure 12 shows that during the first 0.049 seconds, the estimated speed value lags behind the actual value, and after that, the error approaches zero. Figure 13 shows that the estimated rotor electrical angle fits well with the actual electrical angle from the start, indicating that the EKF is able to track the rotor position effectively. Due to the excellent dynamic stability and compensation performance of the ADRC controller, the EKF estimation will become increasingly closer to the actual value as the operating time increases.

7. Experimental Verification

7.1. Experimental Verification

To verify the performance of the controller designed in this paper, an experimental setup was built as shown in Figure 14. The main control chip used is the STM32F407IGT6. The inverter adopts a three-phase bridge inverter circuit. The control board is connected to a PC host via a serial port, allowing real-time transmission of motor parameters to the host for graphical display. The controller is designed and the parameters are tuned as described in the previous sections.

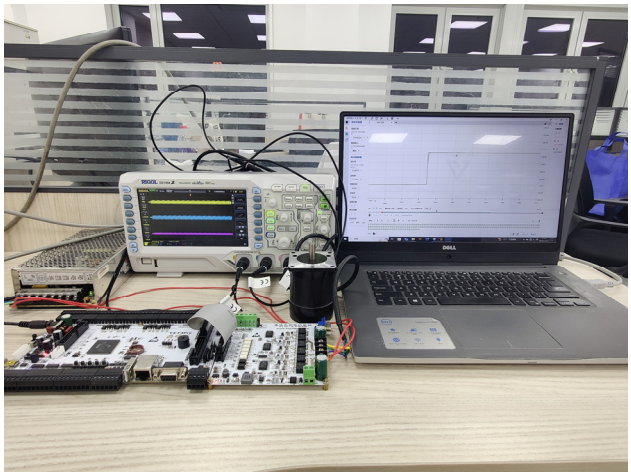

Figure 14. Diagram of the experimental platform

The PMSM motor parameters used in the experiment are shown in Table 5.

Table 5. PMSM Parameter Table

Parameter	Value
Rated power P_e/W	100
Rated voltage V_e/V	24
Rated speed n/RPM	4500
Rated current I_e/A	6
Stator resistance R_s/Ω	0.42
Number of pole pairs P_n	4
Stator inductance L_s/mH	1.24
Rated torque (N·m)	0.38

7.2. Experimental Results

The target speed of the motor is set to 4500 RPM. At 3 seconds, the load is increased by 2 N·m. From 6 seconds to 20 seconds, the target speed of the motor gradually decreases from 4500 RPM to 500 RPM in steps of 1000 RPM, and then stops. The speed waveforms for the LADRC+EKF and NLADRC+EKF systems are shown in Figures 15 and 16, respectively.

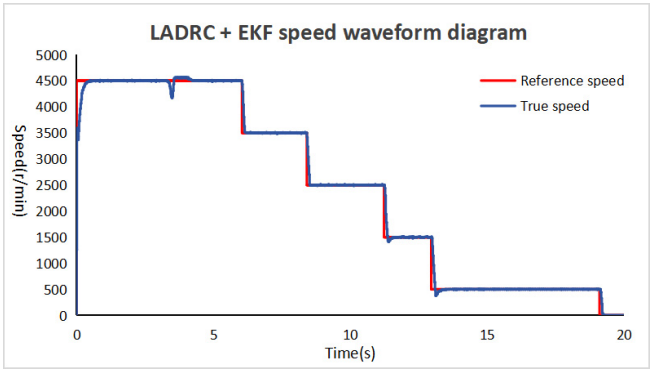

Figure 15. Speed waveform based on LADRC+EKF system

As shown in Figure 15, within the first 6 seconds, when the reference speed is set to 4500 RPM, the LADRC+EKF system exhibits no overshoot, and the speed stabilizes at 4500 RPM in 0.7 seconds. At 3 seconds, a 2 N·m load is applied. The LADRC+EKF system takes 1.2 seconds to return to 4500 RPM, with an overshoot of 4560 RPM during the recovery process. From 6 seconds onwards, the target speed gradually decreases by 1000 RPM steps down to 500 RPM. The LADRC+EKF system follows each speed change in 0.2 seconds. However, when the speed decreases to 1500 RPM and 500 RPM, there is a noticeable overshoot. Subsequently, when the motor stops, the speed change is smooth, and no

reversal occurs.

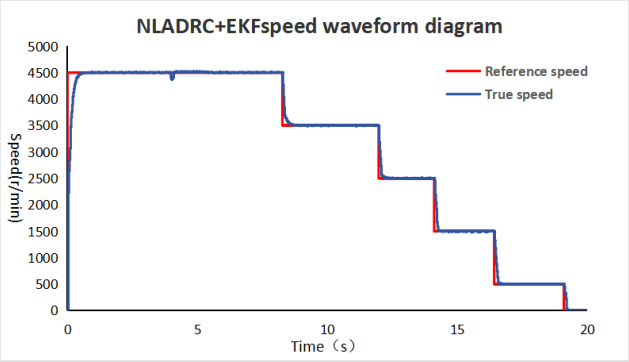

Figure 16. Speed waveform based on NLADRC+EKF system

As shown in Figure 16, within the first 6 seconds, when the reference speed is set to 4500 RPM, the NLADRC+EKF system exhibits no overshoot, and the speed stabilizes at 4500 RPM in 0.9 seconds. At 4 seconds, 2 N·m load is applied. The NLADRC+EKF system takes 0.6 seconds to return to 4500 RPM without any overshoot during the recovery process. From 7 seconds onwards, the target speed gradually decreases by 1000 RPM steps down to 500 RPM. The NLADRC+EKF system follows each speed change in about 0.3 seconds, without overshoot during the process. Subsequently, when the motor stops, the speed change is smooth, and no reversal occurs.

8. Conclusion

This paper focuses on PMSM and proposes two novel sensorless control methods for PMSM by combining the EKF observation algorithm and the Active Disturbance Rejection Control (ADRC) theory. Simulation and experimental results show that both LADRC+EKF and NLADRC+EKF systems outperform the PI+EKF system in terms of disturbance rejection performance, compensation ability, speed regulation range, parameter estimation accuracy, and control precision. The NLADRC+EKF system performs better than the LADRC+EKF system, but its parameter tuning is more complex. The former is suitable for high-precision and high-disturbance rejection scenarios, while the latter is more suitable for general PMSM applications, offering a higher cost-performance ratio and better potential for engineering promotion.

References

[1] Jiang, C., & Jia, H. (2023). Research on vector control system of permanent magnet synchronous motor based on strong tracking EKF. Journal of Combined Machine Tools and Automation Processing Technology, 2023(1), 46-49. https:// doi. org/10.13462/j.cnki.mmtamt.2023.01.011.

[2] Wang S, Jiang C, Tu Q, et al. Particle swarm optimization of fuzzy PI control for PMSMs[J]. Journal of Power Electronics, 2023, 23(10): 1585-1593.

[3] Yang W, Fan Y, Xu D, et al. An improved neural networks-based vector control approach for permanent magnet linear synchronous motor[J]. Journal of the Franklin Institute, 2023.

[4] Liu, L., Cao, X., Qian, M., et al. (2023). Tuning and optimization of the PI controller for current loop in permanent magnet synchronous motor. Journal of Electrical Machines and Control, 27(10), 131-140. https://doi.org/ 10.15938/ j.emc. 2023. 10.013.

[5] Li, J., & Nan, L. (2023). Simulation analysis of adaptive PI control for permanent magnet synchronous motor in electric vehicles. Automobile Practical Technology, 48(8), 22-26. https://doi.org/10.16638/j.cnki.1671-7988.2023.08.004.

[6] Lü, D., Liu, Z., & Xu, X. (2023). Improved MRAS observer control for permanent magnet synchronous motor with load disturbance compensation. Journal of Electrical Machines and Control, 27(6), 46-54. https://doi.org/ 10.15938/ j.emc. 2023. 06.006.

[7] Wang, H., Zhou, B., & Fang, S. (2009). Sliding mode control of permanent magnet synchronous motor speed control system. Transactions of China Electrotechnical Society, 24(9), 71-77. https://doi.org/10.3321/j.issn:1000-6753.2009.09.011.

[8] Li, T. (2022). Robust control method for CNC machine tool permanent magnet synchronous motor using extended sliding mode observer. Manufacturing Technology and Machine Tools, 2022(5), 152-158. https://doi.org/10.19287/j.mtmt.1005-2402. 2022. 05.026.

[9] Han, J. (1989). Control theory--model theory or control theory. Systems Science and Mathematics, (04), 328-335.

[10] Han, J. (1998). Active disturbance rejection controller and its application. Control and Decision, 13(1), 19-23.

[11] Dang, C. (2024). Research on control of permanent magnet synchronous linear motor based on active disturbance rejection strategy [Doctoral dissertation, Lanzhou University of Technology].

[12] Li, L., Ren, Y., Chen, X., & Yin, Z. (2020). Design of MSCSG control system based on ADRC and RBF neural network. Journal of Beijing University of Aeronautics and Astronautics, 1-9. https://doi.org/10.13462/j.buaa.2020.03.14.

[13] Chi, S., & Liu, H. (2023). Active disturbance rejection control of permanent magnet synchronous motor based on feedforward compensation. Journal of Electrical Machines and Control Applications, 50(1), 9-13. https://doi.org/ 10. 12177/ emca. 2022. 141.

[14] Li, Z. (2021). Research on self-tuning strategy of active disturbance rejection control parameters for permanent magnet synchronous motor [Doctoral dissertation, Huazhong University of Science and Technology].

[15] Wang, Y. (2021). Research on active disturbance rejection control of high power density permanent magnet synchronous motor for multi-electric aircraft [Doctoral dissertation, Southeast University].

[16] Zhu, H., & Li, Q. (2020). Design of second-order active disturbance rejection controller for stable platform. Journal of Harbin University of Science and Technology, 25(4), 122-128. https://doi.org/10.15938/j.jhust.2020.04.017.